

CHARACTERIZATION OF A SAMPLE OF INTERMEDIATE-TYPE AGN. I. Spectroscopic properties and serendipitous discovery of new Dual AGN

Erika Benítez¹, Jairo Méndez-Abreu^{2,3}, Isaura Fuentes-Carrera⁴, Irene Cruz-González¹, Benoni
Martínez¹, Luis López-Martin^{2,3}, Elena Jiménez-Bailón¹, Jonathan León-Tavares⁵, Vahram H.
Chavushyan⁶

erika@astro.unam.mx

Received _____; accepted Nov 26 2012

¹Instituto de Astronomía, Universidad Nacional Autónoma de México, Apdo. Postal 70-264, México D.F. 04510, México

²Instituto de Astrofísica de Canarias, 38200 La Laguna, Tenerife, Spain

³Departamento de Astrofísica, Universidad de La Laguna, E-38205 La Laguna, Tenerife, Spain

⁴Escuela Superior de Física y Matemáticas, Instituto Politécnico Nacional (ESFM-IPN), U.P. Adolfo López Mateos, México D.F. 07730, México

⁵Aalto University Metsähovi Radio Observatory, Metsähovintie 114, 02540, Kylmälä, Finland

⁶Instituto Nacional de Astrofísica, Óptica y Electrónica, Apdo. Postal 51-216, 72000 Puebla, México

ABSTRACT

A sample of 10 nearby intermediate-type active galactic nuclei (AGN) drawn from the Sloan Digital Sky Survey (SDSS-DR7) is presented. The aim of this work is to provide estimations of the black hole mass for the sample galaxies from the dynamics of the broad line region. For this purpose, a detailed spectroscopic analysis of the objects was done. Using BPT diagnostic diagrams we have carefully classified the objects as true intermediate-type AGN and found that $80\%_{-17.3\%}^{+7.2\%}$ are composite AGN. The black hole mass estimated for the sample is within $6.54 \pm 0.16 < \log M_{\text{BH}} < 7.81 \pm 0.14$. Profile analysis show that five objects (J120655.63+501737.1, J121607.08+504930.0, J141238.14+391836.5, J143031.18+524225.8 and J162952.88+242638.3) have narrow double-peaked emission lines in both the red ($\text{H}\alpha$, $[\text{N II}]\lambda\lambda 6548, 6583$ and $[\text{S II}]\lambda\lambda 6716, 6731$) and the blue ($\text{H}\beta$ and $[\text{O III}]\lambda\lambda 4959, 5007$) region of the spectra, with velocity differences (ΔV) between the double peaks within $114 < \Delta V < 256$ km s^{-1} . Two of them, J121607.08+504930.0 and J141238.14+391836.5 are candidates for dual AGN since their double-peaked emission lines are dominated by AGN activity. In searches of dual AGN; Type 1, Type 1I and intermediate-type AGN should be carefully separated, due to the high serendipitous number of narrow double-peaked sources ($50\% \pm 14.4\%$) found in our sample.

Subject headings: galaxies: active - galaxies: Seyfert -galaxies: nuclei-quasars:emission lines

1. Introduction

Among nearby active galactic nuclei (AGN) the so-called Seyfert (Sy) galaxies are commonly found. Seyfert galaxies properties were described in the early work by Khachikian & Weedman (1974) who classified them as Sy 1 and Sy 2 depending on the line widths observed in their optical spectra. A few years later, Osterbrock (1981) introduced different sub-classes of Sy galaxies according to the relative intensity showed by the broad emission lines in their spectra. In particular, he introduced the intermediate Sy class, spanning from Sy 1.2 to Sy 1.9. For instance, a Sy 1.8 galaxy shows weak, but readily visible broad $H\alpha$ and $H\beta$ emission lines, while a Sy 1.9 shows only a broad $H\alpha$ component. Recently, Tadhunter (2008) reviewed the general classification and unification of AGN where Sy 1 and Sy 2 galaxies are more generally grouped as Type 1 and Type 2 AGN. Since intermediate-type Sy galaxies do show broad emission line components, they belong to the Type 1 class, but they are more difficult to find since sometimes the intensity of these components can be very low. We will refer to these objects as intermediate-type AGN to distinguish them from the more general Type 1 class.

Early studies on intermediate-type AGN, have proposed that the origin of spectroscopically observed weak emission lines produced in the clouds of the Broad Line Region (BLR) could be explained by internal reddening (Osterbrock 1981; Goodrich 1990, 1995). Another explanation based in the unified model for AGN (Urry & Padovani 1995) assumes that a dusty-torus located some parsecs away from the central source blocks part of the emission. Other possibility is that their weak lines could be due to an intrinsically faint non-thermal continuum emission, maybe due to variations in the ionizing continuum (see Trippe et al. 2010, and references therein).

On the other hand, the availability of high-quality spectra of AGN in the Sloan Digital Sky Survey (SDSS; York et al. 2000) makes it possible to identify intermediate-type AGN and furthermore study them as a class, in order to find their place in the black hole demography for nearby AGN (see Ho 2004). In general, new estimates of fundamental parameters like the

black hole (BH) mass or M_{BH} in AGN can contribute to the understanding of the associated fueling mechanisms. The M_{BH} can be estimated using different empirically calibrated scaling relations in samples designed to study particular types of AGN (e.g. Wandel et al. 1999; Vestergaard & Peterson 2006). In particular, BH mass estimates can be obtained using the correlation between the AGN continuum luminosity (Kaspi et al. 2000, 2005) and BLR radius. By combining continuum luminosity with the width of the $H\beta$ emission line (in objects that have $z < 1$, otherwise this line goes to the IR) it is possible to estimate the mass of the black hole by using a single AGN spectrum, yielding BH masses that are accurate to a factor of ~ 3 (Vestergaard & Peterson 2006).

In the case of intermediate-type AGN, estimates of the M_{BH} need to be done systematically. Previous works in this type of AGN are based on single or very few objects (e.g. Osterbrock 1981; Goodrich 1989; Rafanelli et al. 1993; Xanthopoulos 1996; Popović & Mediavilla 1997; Quillen et al. 2000; Torrealba et al. 2006). A larger amount of objects was recently studied by Trippe et al. (2010). These authors selected a sample of 34 previously classified Sy1.8/1.9 and found that 18 are misclassified objects. Therefore, it is necessary to carefully classify candidates in order to establish if they conform a true sample of intermediate-type AGN.

Among the Type 1 and Type 2 AGN samples drawn from the SDSS, the sample of double-peaked narrow emission line AGN stands out. Usually they show [O III] line profiles with velocities splitting in the range 151 to 1314 km s^{-1} . The relevance of studying these kind of AGN is based on the idea that they are candidates for sub-kpc or kpc-scale dual AGN (e.g. Comerford et al. 2009). Discovering new dual (or binary, if their nuclei appears separated on pc-scales) AGN candidates is fundamental to constrain models of galaxy formation and evolution. Since it is commonly believed that mergers can trigger or enhance nuclear accretion, it is fundamental to establish their frequency by means of detecting dual or binary AGN. Nevertheless, it is a fact that direct observational evidence for binary super massive black holes still remains

scarce (see McGurk et al. 2011, and references therein).

Double-peaked [O III] line profiles could arise from several mechanisms (e.g., Xu & Komossa 2009; Rosario et al. 2010; Fu et al. 2011a; Shen et al. 2011): (1) the orbital motion of a binary AGN, (2) gas kinematics in extended narrow-line regions, and (3) unresolved nuclear gas kinematics (e.g., aligned outflows or disk rotation on small scales). Fu et al. (2011b) have obtained high-resolution imaging of 106 narrow double-peaked AGN (37 Type 1 and 69 Type 1I) and found that 31 have companions within 3". Their integral field spectroscopic observations has allowed them to group the narrow double-peaked AGN in the above three broad categories, according to the origin of the double-peaked [O III] line profiles, finding that only 4.5-12 % are binaries. Other studies on the frequency of these objects among AGN (e.g., Wang et al. 2009; Liu et al. 2010; Smith et al. 2010) have show that there are 340 objects between $0.008 < z < 0.686$ or, equivalently, ~ 1 % of the entire SDSS AGN sample harboring possible dual AGN. Nevertheless, a recent study done by Fu et al. (2012) shows that several objects classified in the literature as “binary” are, most likely, single AGN with extended narrow-line regions. Therefore, the frequency of double-peak objects and binaries among intermediate-type AGN are still unknown, and so this is worth to investigate.

The aim of this work is to isolate intermediate-type AGN objects and estimate their black hole mass. In particular, we are interested in providing new estimates that can contribute to the study of the black hole demography in nearby AGN. For this purpose, we present the spectral analysis of a sample of 10 nearby ($10^{42} \lesssim L_{\text{bol}} \lesssim 10^{44} \text{erg s}^{-1}$) intermediate-type AGN (i.e. intermediate Sy galaxies). Spectral analysis will provide a more precise classification through the use of the Baldwin-Phillips-Terlevich (BPT) diagnostic diagrams. A detailed profile decomposition allowed us to discover new narrow double-peaked AGN candidates among the objects in the sample.

The paper is organized as follows: In Sect. 2 we describe the sample selection and in Sect. 3 the analysis of the SDSS spectroscopic data. Sect. 4 shows the results obtained for the sample and

relevant properties of some individual objects. The discussion and conclusions are presented in Sect. 5. An Appendix on the available X-ray data for one of the selected sources is presented. The cosmology adopted for this work is $H_0 = 70 \text{ km s}^{-1} \text{ Mpc}^{-1}$, $\Omega_m = 0.3$ and $\Omega_\lambda = 0.7$.

2. Sample Selection

We selected objects flagged as quasars (QSO) in the SDSS database that have Petrosian g -band magnitudes between $14 \lesssim m_g \lesssim 17$ and redshifts within $0.026 < z < 0.12$, i.e., a sample of nearby AGN. From this sample, we chose only those galaxies that have spectroscopic data in the SDSS database in order to accurately obtain their spectral classification. An additional condition imposed was that visually all selected galaxies should have spectral characteristics of intermediate-type AGN. We ended up with a sample of 23 candidates that were photometrically observed with the Nordic Optical Telescope (NOT). Results obtained with these data are presented in a companion paper (Benítez et al. 2012b, hereafter Paper II). A final sample of 10 candidates for intermediate-type AGN were chosen for this work, these are presented in Table 1. The remaining objects were taken out from the sample since after a preliminary analysis of their spectra, we found that some of them were either narrow line Seyfert 1 (Osterbrock & Pogge 1985) or Seyfert 1 objects.

3. Analysis of SDSS-DR7 spectra

The optical SDSS-DR7 spectra of our sample were processed using the STARLIGHT code (Cid Fernandes et al. 2005; Mateus et al. 2006). This code has been successfully used to study some AGN samples (see Bian et al. 2007; Stasińska et al. 2006; Rafanelli et al. 2009; Cid Fernandes et al. 2011; Coziol et al. 2011; Mezcua et al. 2011; León-Tavares et al. 2011). In a first run, all spectra were corrected for Galactic extinction using the dust maps of Schlegel et al.

(1998) and the extinction law of Cardelli et al. (1989). Also in this first run, in order to obtain the signal-to-noise ratio (S/N) we have masked the most prominent emission lines that are known to be present in the composite spectra of QSOs (see Francis et al. 1991). So, the following lines were masked: [O II] $\lambda\lambda$ 3726,3729, [Ne III] λ 3869, H ϵ λ 3970, H δ λ 4102, H γ λ 4340, H β λ 4861, [O III] $\lambda\lambda$ 4959,5007, He I λ 5876, [O I] λ 6300, H α λ 6562, [N II] $\lambda\lambda$ 6548,6583, and [S II] $\lambda\lambda$ 6717,6731; together with the ISM absorption from Na D λ 5890 Å). The signal-to-noise ratio (S/N) was obtained for each spectrum in the wavelength range of 4730 to 4780 Å and is presented in Col. 2 of Table 2.

Based on the S/N previously obtained, each spectrum was randomly perturbed 100 times using a Monte Carlo (MC) seed. Our lowest S/N value was 5.9, so the perturbations varied $\pm 16\%$ of the signal value. We obtained 100 simulated spectra per object that were also analyzed with STARLIGHT, masking again the prominent emission lines as we did in the first run. From these simulated spectra, we obtained a collection of 100 models for the absorption spectrum of the host galaxy, from which we will obtain an estimation of the velocity dispersion. We chose the median of the distribution of models as our best model of the host-galaxy absorption spectrum. The stellar velocity dispersion σ_* was estimated from the median value of the distribution and the quoted errors are the rms values (see Table 5). In all cases the obtained σ_* is larger than 65 km s^{-1} , which is the nominal SDSS velocity resolution (e.g., Liu et al. 2010). The AGN continuum flux at 5100 Å was estimated from the the collection of 100 power-law fittings. Again we chose the best fit from the median value of the distribution of models to obtain $F_{5100 \text{ Å}}$ and the rms as the associated error. This flux will be used to derive the BH mass, as is described in Sect. 4.1. Therefore, STARLIGHT provided us with the best synthetic spectra for our AGN sample.

The original SDSS spectra and the final pure AGN spectra, together with the obtained fits for the sample objects are shown in Figs. 1 to 5. These figures show how the stellar contribution is subtracted with STARLIGHT from the composite spectra. This is essential for our study since

the absorption synthetic spectra were used to estimate the velocity dispersion and the pure AGN spectra to perform a line profile analysis. An example of the best model obtained for object #9 is shown in Figure 6, where it can be seen how STARLIGHT is capable to fit the absorption lines used to estimate the velocity dispersion along with the stellar continuum. The absorption lines used to estimate σ_* are marked in the blow-up spectrum.

The complete optical spectroscopic parameters obtained for the sample are presented in Table 2. The FWHM for both the H α and H β broad components have errors <10%. The line ratios have also errors <10% except for object #10 that has errors \sim 18%. The profile decomposition in all cases was done using the algorithm PeakFit¹. From our profile decomposition analysis, we find that in five objects (#1, #3, #4, #5 and #8) the [O III] $\lambda\lambda$ 4959,5007, [S II] $\lambda\lambda$ 6716,6731, [N II] $\lambda\lambda$ 6548,6583 doublets and the narrow components of H α and H β clearly show a double-peaked profile. The spectral profile decomposition of these five narrow-double peaked AGN are shown in Figs. 7 to 11. We have checked the redshifts using some absorption lines from the host galaxy spectra and found that they are in good agreement with the values reported in NED², which are based mainly on emission lines. Therefore, the Gaussians centroids were forced to correspond to the host galaxy redshift. For all objects, the widths of the Gaussians fitted to the narrow lines have the same Doppler broadening, and the intensity ratio [O III] λ 5007/[O III] λ 4959 was fixed to its theoretical value. Table 3 presents the velocity difference defined as $\Delta V = V_{\text{red}} - V_{\text{blue}}$ for each object with double-peaked narrow emission lines for various lines.

Baldwin et al. (1981) propose a suite of diagnostic diagrams (known as BPT) to classify emission-line galaxies in order to disentangle the dominant energy source. The diagrams are based

¹Systat Software Inc. <http://www.sigmaplot.com>

²The NASA/IPAC Extragalactic Database (NED) is operated by the Jet Propulsion Laboratory, California Institute of Technology, under contract with the National Aeronautics and Space Administration.

on four optical line ratios $[\text{O III}]/\text{H}\beta$, $[\text{N II}]/\text{H}\alpha$, $[\text{S II}]/\text{H}\alpha$ and $[\text{O I}]/\text{H}\alpha$. Following Kewley et al. (2006), we present in Figure 12 two BPT diagnostic diagrams that show the location of the sample objects. These diagrams used line ratios $[\text{O III}]/\text{H}\beta$, $[\text{N II}]/\text{H}\alpha$ and $[\text{S II}]/\text{H}\alpha$.

We note that for the narrow double-peaked objects we present the obtained line ratios separately using the blue and red components. This allowed us to see how objects can change their spectral classification in the diagnostic diagram. We have found that 8 objects are composite AGN (Starburst plus AGN). In Table 5 we present the spectral classification obtained for all objects. In some objects we obtained different classifications since they appear in different places in the two BPT diagrams. In particular, object #2 appears as a Starburst (SB) galaxy in one of the BPT diagrams. In addition, since all objects present a broad line component, and following Whittle (1992), we have obtained their Sy type based on $F_{5007}/F_{\text{H}\beta} = R$. Then, we have assigned Sy 1 ($R \leq 0.3$), Sy 2 ($0.3 < R \leq 1$), Sy 1.5 ($1 < R \leq 4$), Sy 1.8 ($R > 4$), and Sy 1.9 if only broad $\text{H}\alpha$ was seen.

4. Results

4.1. M_{BH} estimates

The M_{BH} for all objects in the sample were indirectly derived using an empirically calibrated photoionization method (Wandel et al. 1999; Vestergaard 2002; Vestergaard & Peterson 2006). We derived BH masses using the SDSS-DR7 spectra using equation 5 from Vestergaard & Peterson (2006), which makes use of the FWHM of the $\text{H}\beta$ emission-line and the continuum luminosity at 5100 \AA . Luminosity at 5100 \AA (L_{5100}) was estimated from the median flux derived with the power-law fit done with STARLIGHT and the luminosity distances of the objects using the redshifts given in NED. The bolometric luminosity was obtained using $L_{\text{bol}} \sim 9\lambda L_{\lambda 5100}$ (see Kaspi et al. 2000), which yields the Eddington ratio $L_{\text{bol}}/L_{\text{Edd}}$, where $L_{\text{Edd}} \approx 1.3 \times 10^{38} (M_{\text{BH}}/M_{\odot})$.

Our luminosity results are shown in Table 4. For objects without H β broad component, the H α line FWHM was converted to H β FWHM using equation 3 given by Shen et al. (2008). The BH mass estimates for our sample are shown in Table 5.

We can also derive the BH mass using the so called M- σ_* relation (Ferrarese & Merritt 2000; Gebhardt et al. 2000) and see if these estimates are in agreement with the black hole mass derived for these objects using scaling relations. This is the reason why we obtained the velocity dispersion (σ_*) with STARLIGHT. However, since the use of this relation depends on the bulge type associated with the host galaxy (e.g. Hu 2008), we will present these estimates in Paper II, along with a detailed discussion of the bulge type present in each galaxy based on the photometric and spectroscopic observations.

In Fig. 13 we show the BH mass vs. luminosity relation obtained for the objects in our sample. The diagonal lines show the Eddington limits shown by our objects. Note that internal extinction has not been taken into account. All objects have low to moderate accretion Eddington rates ($L_{\text{bol}}/L_{\text{Edd}} < 0.11$).

4.2. Double-Peaked Objects

Spectral analysis showed that among our objects we have five objects that clearly show narrow double-peaked emission lines: galaxies #1, #3, #4, #5 and #8 (c.f. Table 1). In Table 3 we present the velocity differences, $\Delta V = V_{\text{red}} - V_{\text{blue}}$, for H α , [N II] λ 6548, [N II] λ 6583, [S II] λ 6716, [S II] λ 6731, H β , [O III] λ 4959, and [O III] λ 5007 lines. Our definition of a narrow line double-peaked object requires that in all these lines a double-peaked Gaussian components should be present. The average values and standard deviation obtained for each source are listed in the bottom line of this table, which shows that they are within $114 \lesssim \Delta V \lesssim 256 \text{ km s}^{-1}$.

4.3. Notes on particular objects

4.3.1. *J120655.63+501737.1 (#1)*

The profile decomposition shows that this AGN was best fitted using double-peaked lines for its narrow line region (NLR, see Fig. 7). Its spectrum was fitted with a broad component for the $H\beta$ and $H\alpha$ lines, and from its locus in the BPT diagrams shown in Fig. 12, we classify this object as a composite AGN. The blue component indicates that it is a Sy 1.8+SB, and the red component that it is a Sy 1.5 + SB.

4.3.2. *J121600.04+124114.3 (#2)*

In Véron-Cetty & Véron (2010) and in NED this object is classified as a Sy 1.9, and in Mazzarella & Balzano (1986) it is classified as a Starburst (SB) galaxy. We agree with both classifications since this object appears in one diagram as a composite Sy 1.9 + SB, and in the other as a clear Starburst galaxy, c.f., Fig. 12. We noted that the emission line fitting of this object clearly needed a double-peaked Gaussian component for [O III], [S II] and [N II] lines; but when fitting the narrow components of $H\alpha$ and $H\beta$ only one Gaussian component was required. Since we did not needed double-peaked Gaussians to fit the narrow line components of $H\alpha$ and $H\beta$, this object was not classified as double-peaked.

4.3.3. *J121607.08+504930.0 (#3)*

The profile decomposition analysis shows that this object is a narrow-line double-peaked AGN, see Fig. 8. Its spectrum was fitted with a broad component for the $H\beta$ and $H\alpha$ lines, and from the locus of each component in the BPT diagnostic diagrams shown in Fig. 12, we classify this object as a Sy 1.8 galaxy.

4.3.4. *J141238.14+391836.5 (#4)*

From our profile decomposition, we find that this AGN is a narrow-line double-peaked (Fig. 9) source. In addition, we noted that this object lacks a broad component in the $H\beta$ region. From its locus in the BPT diagrams in Fig. 12, and using the blue and the red components, we classify this object as a Sy 1.9 galaxy.

4.3.5. *J143031.18+524225.8 (#5)*

This object is also a narrow-line double-peaked source, see Fig. 10. Since we need a broad Gaussian component to fit the $H\alpha$ region, and from the BPT diagnostic diagrams in Fig. 12, using both the blue and red components we classify this object as a Sy 1.5 + SB.

4.3.6. *J162952.88+242638.3 (#8)*

The $[\text{O III}]\lambda\lambda 4949,5007$ doublets clearly show a double-peaked profile and a rather broad wing. We fitted the profile with two sets of three Gaussians. Two Gaussian profiles were used for fitting the narrow component of $H\beta$ (Fig. 11). The profile decomposition shows a broad Gaussian component for $H\alpha$. The BPT diagnostic diagrams in Fig. 12 clearly show that, using both red and blue components, the object is a composite AGN and we classify it as a Sy 1.9 + SB. The results on the spectral analysis of the XMM-Newton data on this source (see Appendix A) are in agreement with the optical data ones. This is based on the obtained value of the Γ index and the low values found for the equivalent N_H . Both values are compatible with Type I objects (e.g., Piconcelli et al. 2005).

5. Discussion and Conclusions

The sample presented in this work consists of ten nearby intermediate-type AGN, some of them showing a weak broad $H\alpha$ line component. An example of this was presented in the profile analysis of J162952.88+242638.3. It clearly shows a rather weak broad component in $H\alpha$ (cf. Fig. 11), typical of a Sy 1.9 galaxy. This result is also supported with our analysis of the XMM public available data on this object that showed that the power index and the hydrogen column absorption are compatible with Type 1 (c.f., Appendix A) objects. Thus, our Sy 1.9 classification for this object resulted to be in disagreement with Trippe et al. (2010), that recently classify this object as a Seyfert 2 using the same optical and XMM data.

The BPT diagnostic diagram $[O\ III]/H\beta$ vs. $[S\ II]/H\alpha$ clearly shows that all single-peaked objects are composite AGN. In the case of the narrow line double-peaked objects detected in this work, three are composite AGN (#1, #5, and #8) and only two of them (#3 and #4) are pure intermediate Sy galaxies. Therefore, $80\%^{+7.2\%}_{-17.3\%}$ of our intermediate-type objects are composite AGN. It is interesting to note that using the Whittle (1992) classification for intermediate Sy galaxies, we confirm that all objects studied in this work are intermediate-type AGN.

The FWHM of $H\beta$ component was used to estimate the BH mass in all objects for the first time. We found that the sample studied in this work has a BH mass range of $6.54\pm 0.16 < \log M_{BH} < 7.81\pm 0.14$. In particular three objects (#5, #9, and #10) have $M_{BH} \sim 10^6 M_{\odot}$. Recently, Kormendy et al. (2011) suggested that small black holes in bulgeless galaxies or pseudobulges grow as low-level Sy. This idea will be explored in our companion Paper II, where we study the bulge properties of this sample. Also, in Paper II the M_{BH} estimates obtained in this work will be compared with estimates for the same sample through the use of the $M-\sigma_{\star}$ correlation. We also found that objects in our sample have low to moderate accretion rates that go from $(0.21\pm 0.23)\times 10^{-2}$ to $(3.44\pm 0.24)\times 10^{-2}$ and are located at the low-tail of bolometric AGN luminosities.

Among the intermediate-type AGN identified in this sample, $50\% \pm 14.4\%$ show narrow double-peaked emission lines. From the BPT diagrams and following Comerford et al. (2009) we find that two objects #3 and #4 are good candidates for dual AGN since both the blue and red emission line components are dominated exclusively by AGN activity. The other three narrow-double peaked objects #1, #5 and #8 show one emission line component in the AGN region while the other appears in the composite AGN + SB region. Therefore, the precise classification of each component in the case of double-peaked AGN is essential, since it gives hints on the origin of the observed narrow double-peaked lines. This information could be useful in identifying new dual AGN.

The objects showing narrow double-peaked emission lines found in this work need to be studied through observations enabling spatially resolved imaging and spatially resolved spectroscopy. In searches of dual AGN, Type 1, Type 2 and intermediate-type AGN should be carefully separated, due to the high serendipitously number of narrow double-peaked sources found in our sample. These objects could be useful for establishing the properties and origin of narrow double-peaked emission lines profile in cases where the peak velocity separation lies below 300 km s^{-1} .

We want to thank the anonymous referee for useful suggestions and constructive criticism. We also want to thank Dr. D. Clark who carefully read the final version of the manuscript. EB and BM acknowledges financial support from UNAM-DGAPA-PAPIIT through grant IN116211. JMA is partially funded by the Spanish MICINN under the Consolider-Ingenio 2010 Program grant CSD2006-00070 and also by the grants AYA2007-67965-C03-01 and AYA2010-21887-C04-04. IFC thanks the financial support from CONACYT grant 0133520 and IPN-SIP grant 20121700. Funding for the Sloan Digital Sky Survey (SDSS) and SDSS-II has been provided by the Alfred P. Sloan Foundation, the Participating Institutions, the National Science Foundation, the U.S. Department of Energy, the National Aeronautics and Space Administration, the Japanese

Monbukagakusho, and the Max Planck Society, and the Higher Education Funding Council for England. The SDSS Web site is <http://www.sdss.org/>. This research has made use of the NASA/IPAC Extragalactic Database (NED) which is operated by the Jet Propulsion Laboratory, California Institute of Technology, under contract with the National Aeronautics and Space Administration.

REFERENCES

- Baldwin, J. A., Phillips, M. M., & Terlevich, R. 1981, *PASP*, 93, 5
- Bian, W.-H., Chen, Y.-M., Gu, Q.-S., & Wang, J.-M. 2007, *ApJ*, 668, 721
- Cardelli, J. A., Clayton, G. C., & Mathis, J. S. 1989, *ApJ*, 345, 245
- Cid Fernandes, R., Mateus, A., Sodré, L., Stasińska, G., & Gomes, J. M. 2005, *MNRAS*, 358, 363
- Cid Fernandes, R., Stasińska, G., Mateus, A., & Vale Asari, N. 2011, *MNRAS*, 413, 1687
- Comerford, J. M., Griffith, R. L., Gerke, B. F., Cooper, M. C., Newman, J. A., Davis, M., & Stern, D. 2009, *ApJ*, 702, L82
- Coziol, R., Torres-Papaqui, J. P., Plauchu-Frayn, I., Islas-Islas, J. M., Ortega-Minakata, R. A., Neri-Larios, D. M., & Andernach, H. 2011, *Rev. Mexicana Astron. Astrofis.*, 47, 361
- Ferrarese, L., & Merritt, D. 2000, *ApJ*, 539, L9
- Francis, P. J., Hewett, P. C., Foltz, C. B., Chaffee, F. H., Weymann, R. J., & Morris, S. L. 1991, *ApJ*, 373, 465
- Fu, H., Myers, A. D., Djorgovski, S. G., & Yan, L. 2011a, *ApJ*, 733, 103
- Fu, H., Yan, L., Myers, A. D., Stockton, A., Djorgovski, S. G., Aldering, G., & Rich, J. A. 2011b, *ArXiv* 1107.3564
- . 2012, *ApJ*, 745, 67
- Gabriel, C., et al. 2004, in *Astronomical Society of the Pacific Conference Series*, Vol. 314, *Astronomical Data Analysis Software and Systems (ADASS) XIII*, ed. F. Ochsenbein, M. G. Allen, & D. Egret, 759
- Gebhardt, K., et al. 2000, *ApJ*, 539, L13

Goodrich, R. W. 1989, *ApJ*, 340, 190

—. 1990, *ApJ*, 355, 88

—. 1995, *ApJ*, 440, 141

Ho, L. C. W. 2004, *Coevolution of Black Holes and Galaxies*, 292

Hu, J. 2008, *MNRAS*, 386, 2242

Kaspi, S., Maoz, D., Netzer, H., Peterson, B. M., Vestergaard, M., & Jannuzi, B. T. 2005, *ApJ*, 629, 61

Kaspi, S., Smith, P. S., Netzer, H., Maoz, D., Jannuzi, B. T., & Giveon, U. 2000, *ApJ*, 533, 631

Kauffmann, G., et al. 2003, *MNRAS*, 346, 1055

Kendall, M., & Stuart, A. 1977, *The advanced theory of statistics. Vol.1: Distribution theory*, ed. Kendall, M. & Stuart, A.

Kewley, L. J., Dopita, M. A., Sutherland, R. S., Heisler, C. A., & Trevena, J. 2001, *ApJ*, 556, 121

Kewley, L. J., Groves, B., Kauffmann, G., & Heckman, T. 2006, *MNRAS*, 372, 961

Khachikian, E. Y., & Weedman, D. W. 1974, *ApJ*, 192, 581

Kormendy, J., Bender, R., & Cornell, M. E. 2011, *Nature*, 469, 374

León-Tavares, J., Valtaoja, E., Chavushyan, V. H., Tornikoski, M., Añorve, C., Nieppola, E., & Lähteenmäki, A. 2011, *MNRAS*, 411, 1127

Liu, X., Shen, Y., Strauss, M. A., & Greene, J. E. 2010, *ApJ*, 708, 427

Mateus, A., Sodr e, L., Cid Fernandes, R., Stasińska, G., Schoenell, W., & Gomes, J. M. 2006, *MNRAS*, 370, 721

- Mazzarella, J. M., & Balzano, V. A. 1986, *ApJS*, 62, 751
- McGurk, R. C., Max, C. E., Rosario, D. J., Shields, G. A., Smith, K. L., & Wright, S. A. 2011, *ApJ*, 738, L2
- Mezcua, M., Lobanov, A. P., Chavushyan, V. H., & León-Tavares, J. 2011, *A&A*, 527, A38
- Osterbrock, D. E. 1981, *ApJ*, 249, 462
- Osterbrock, D. E., & Pogge, R. W. 1985, *ApJ*, 297, 166
- Piconcelli, E., Jimenez-Bailón, E., Guainazzi, M., Schartel, N., Rodríguez-Pascual, P. M., & Santos-Lleó, M. 2004, *MNRAS*, 351, 161
- . 2005, *A&A*, 432, 15
- Popović, L. Č., & Mediavilla, E. 1997, *Publications de l'Observatoire Astronomique de Beograd*, 57, 95
- Quillen, A. C., Shaked, S., Alonso-Herrero, A., McDonald, C., Lee, A., Rieke, M. J., & Rieke, G. H. 2000, *ApJ*, 532, L17
- Rafanelli, P., D'Abrusco, R., Ciroi, S., Cracco, V., di Mille, F., & Vaona, L. 2009, *New A Rev.*, 53, 186
- Rafanelli, P., Marziani, P., Birkle, K., & Thiele, U. 1993, *A&A*, 275, 451
- Rosario, D. J., Shields, G. A., Taylor, G. B., Salviander, S., & Smith, K. L. 2010, *ApJ*, 716, 131
- Schlegel, D. J., Finkbeiner, D. P., & Davis, M. 1998, *ApJ*, 500, 525
- Shen, J., Vanden Berk, D. E., Schneider, D. P., & Hall, P. B. 2008, *AJ*, 135, 928
- Shen, Y., Liu, X., Greene, J. E., & Strauss, M. A. 2011, *ApJ*, 735, 48

- Smith, K. L., Shields, G. A., Bonning, E. W., McMullen, C. C., Rosario, D. J., & Salviander, S. 2010, *ApJ*, 716, 866
- Stasińska, G., Cid Fernandes, R., Mateus, A., Sodré, L., & Asari, N. V. 2006, *MNRAS*, 371, 972
- Tadhunter, C. 2008, *New Astronomy Reviews*, 52, 227
- Torrealba, J., Benítez, E., Franco-Balderas, A., & Chavushyan, V. H. 2006, *RevMexAA*, 42, 3
- Trippe, M. L., Crenshaw, D. M., Deo, R. P., Dietrich, M., Kraemer, S. B., Rafter, S. E., & Turner, T. J. 2010, *ApJ*, 725, 1749
- Urry, C. M., & Padovani, P. 1995, *PASP*, 107, 803
- Véron-Cetty, M., & Véron, P. 2010, *A&A*, 518, A10+
- Vestergaard, M. 2002, *ApJ*, 571, 733
- Vestergaard, M., & Peterson, B. M. 2006, *ApJ*, 641, 689
- Wandel, A., Peterson, B. M., & Malkan, M. A. 1999, *ApJ*, 526, 579
- Wang, J.-M., Chen, Y.-M., Hu, C., Mao, W.-M., Zhang, S., & Bian, W.-H. 2009, *ApJ*, 705, L76
- Whittle, M. 1992, *ApJS*, 79, 49
- Xanthopoulos, E. 1996, *MNRAS*, 280, 6
- Xu, D., & Komossa, S. 2009, *ApJ*, 705, L20
- York, D. G., et al. 2000, *AJ*, 120, 1579

A. XMM DATA ANALYSIS OF J162952.88+242638.3 (#8)

We searched for X-ray data available for our sample objects in Chandra and XMM-Newton databases. We found that only one of our objects has been observed with XMM-Newton. This object is J162952.88+242638.3, also known as Mrk 883. The three XMM-Newton observations analyzed for this object were performed during August 13th, 15th and 21st 2006 (Obs. ID 0302260101; 0302260701 and 0302261001, respectively). The exposure times after flare removal (see below) were 7.9, 10.5 and 10.5 ks. All the observations were processed using the standard Science Analysis System, SAS v10.3.0 (Gabriel et al. 2004) and using the most updated calibration files available in January 2011. The EPIC-pn events were filtered due to high background events using the method described in Piconcelli et al. (2004). No signs of pile-up or out-of-time events were detected in any of the observations.

The spectra of each observation were extracted from circles centered in the maximum emission pixel and with radii which maximized the signal-to-noise, i.e., 22.5 ". The background circular regions used for the spectral analysis were located close to the source and free of any contaminating source. Both response matrices were generated for each observation using `arfgen` and `remgen` SAS (<http://xmm.esac.esa.int/sas/>) tasks. The spectra were binned to have at least 20 counts per bin in order to be able to use the modified χ^2_ν technique (Kendall & Stuart 1977) for the data fit. All the three spectra were analyzed simultaneously. The shape of the continuum is quite similar among the three observations, with a slight increment of the emission for the third observation. After taking into account the absorption due to our Galaxy, $N_H=3.83 \times 10^{20} \text{cm}^{-2}$, the continuum emission can be satisfactorily fitted with a single absorbed power-law with a photon index $\Gamma=1.7\pm 0.03$ and an equivalent hydrogen column density of the order of $1 \times 10^{21} \text{cm}^{-2}$. Table 6 summarizes the values of the parameters for the best fit model.

None of the observations of this object present an iron line statistically significant, although both a neutral iron line with the energy fixed to 6.4 keV and an iron line with the energy left

free to vary were tested. During the eight days in which the observations span, moderate flux variability between the two first observations and the last one was detected. Neither power-law index nor intrinsic absorption variation were measured. Figure 14 summarizes the results for the X-ray analysis of SDSS J162953.88+242638.3: the best-fit model for the three spectra with the residuals to the data, and the contour plots for the confidence level between the Γ index and the equivalent N_H for the three observations.

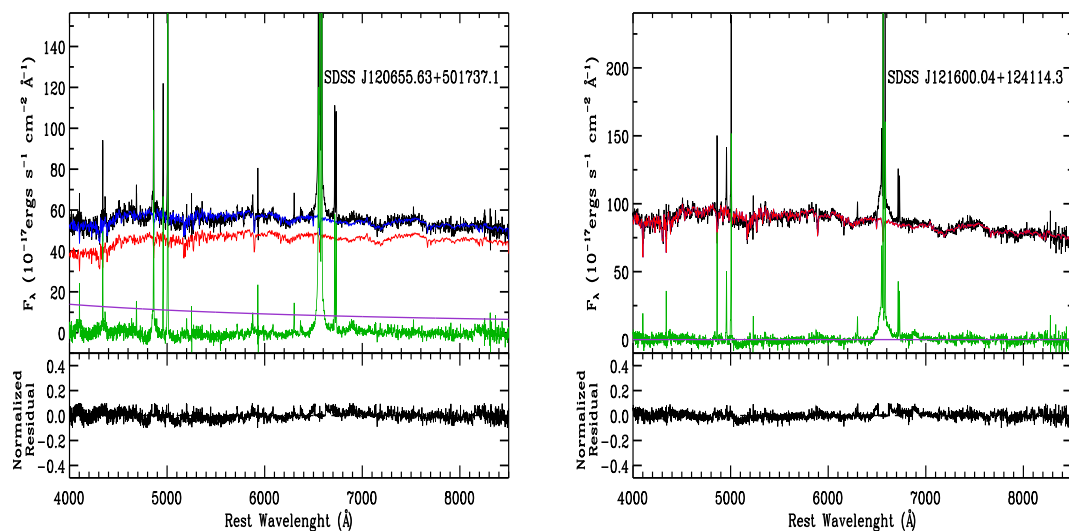


Fig. 1.— STARLIGHT fit of the SDSS spectra. The black line shows the original SDSS de-redshifted spectrum. The red line shows the pure stellar continuum spectrum and the purple line the power-law used to fit the AGN continuum. The blue line shows the best fit to the data and represents the sum of the red spectrum plus the AGN continuum. We show in green the final pure AGN spectra of J120655.63+501737.1 and J121600.04+1241143. Bottom panels show the normalized residuals.

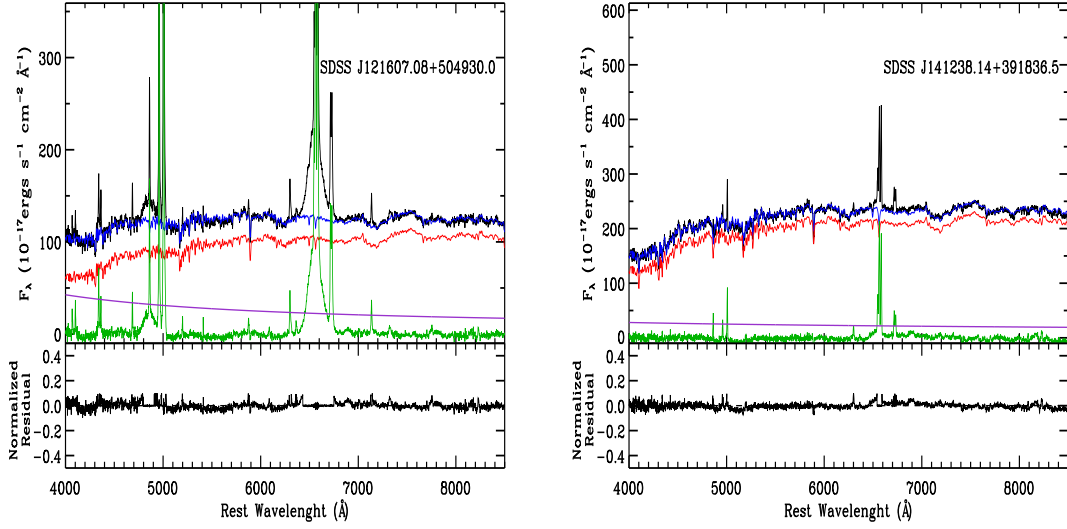


Fig. 2.— Spectra of J121607.08+504930.0 and J141238.14+391836.5. As in Fig. 1.

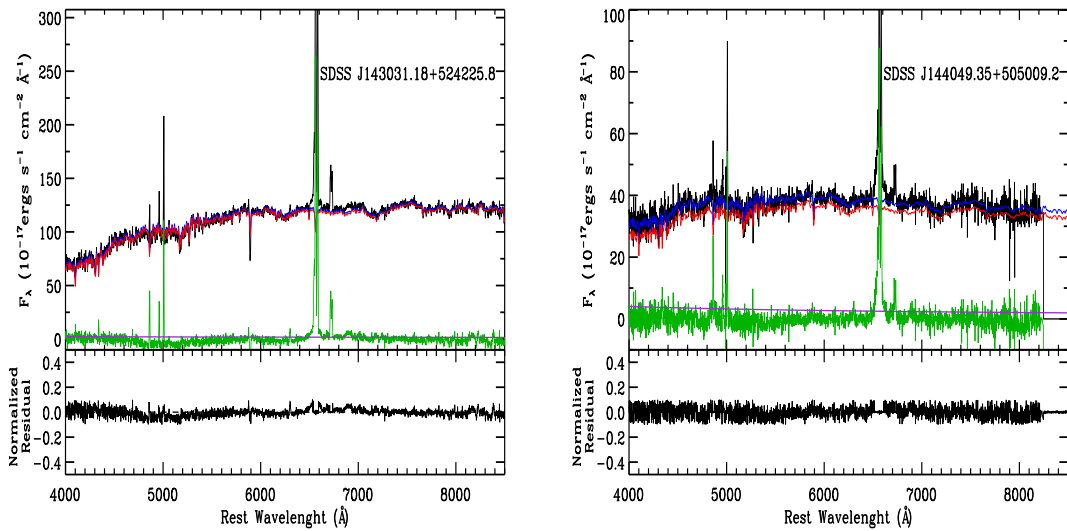


Fig. 3.— Spectra of J143031.18+524225.8 and J144049.35+505009.2. As in Fig. 1.

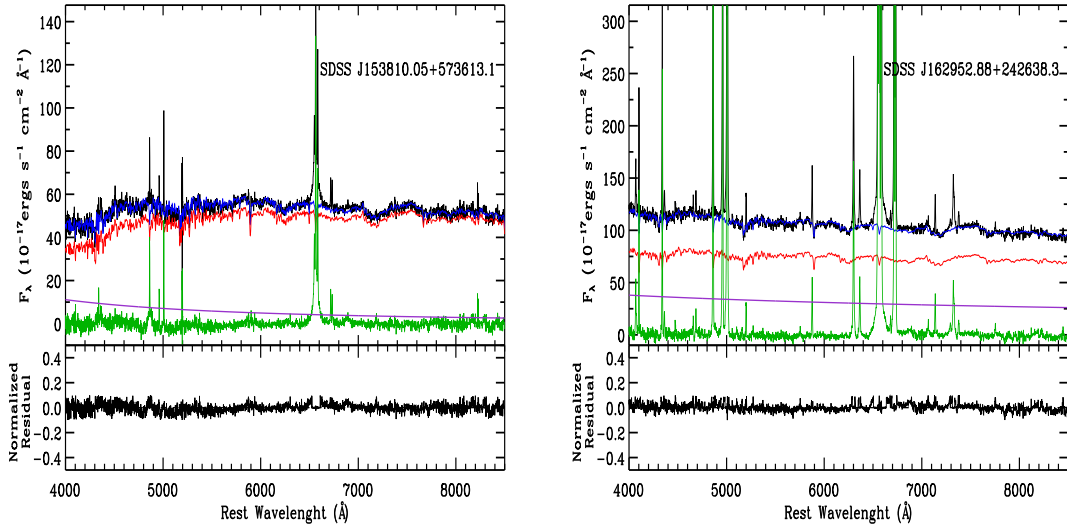


Fig. 4.— Spectra of J153810.05+573613.1 and J162952.88+242638.3. As in Fig. 1.

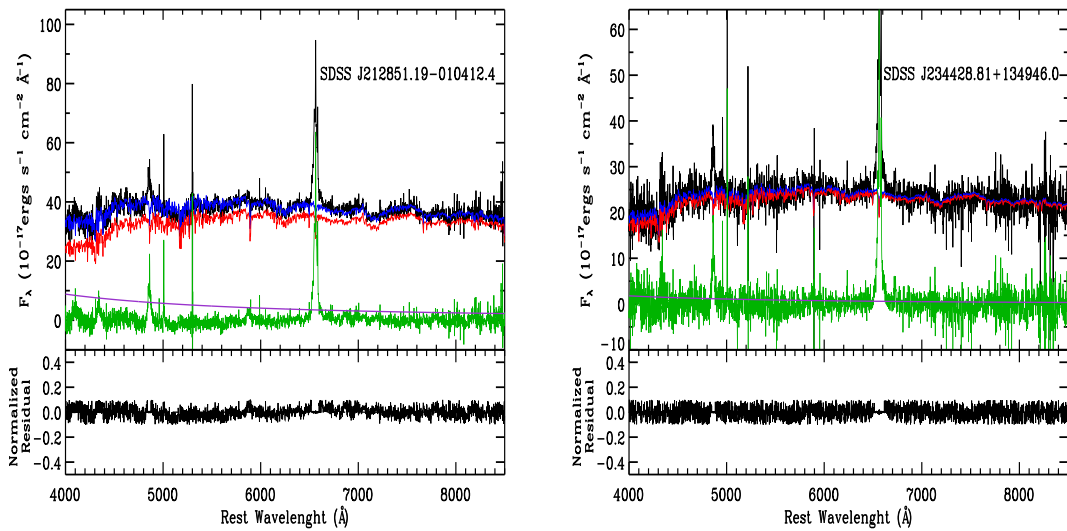


Fig. 5.— Spectra of J212851.19-010412.4 and J234428.81+134946.0. As in Fig. 1.

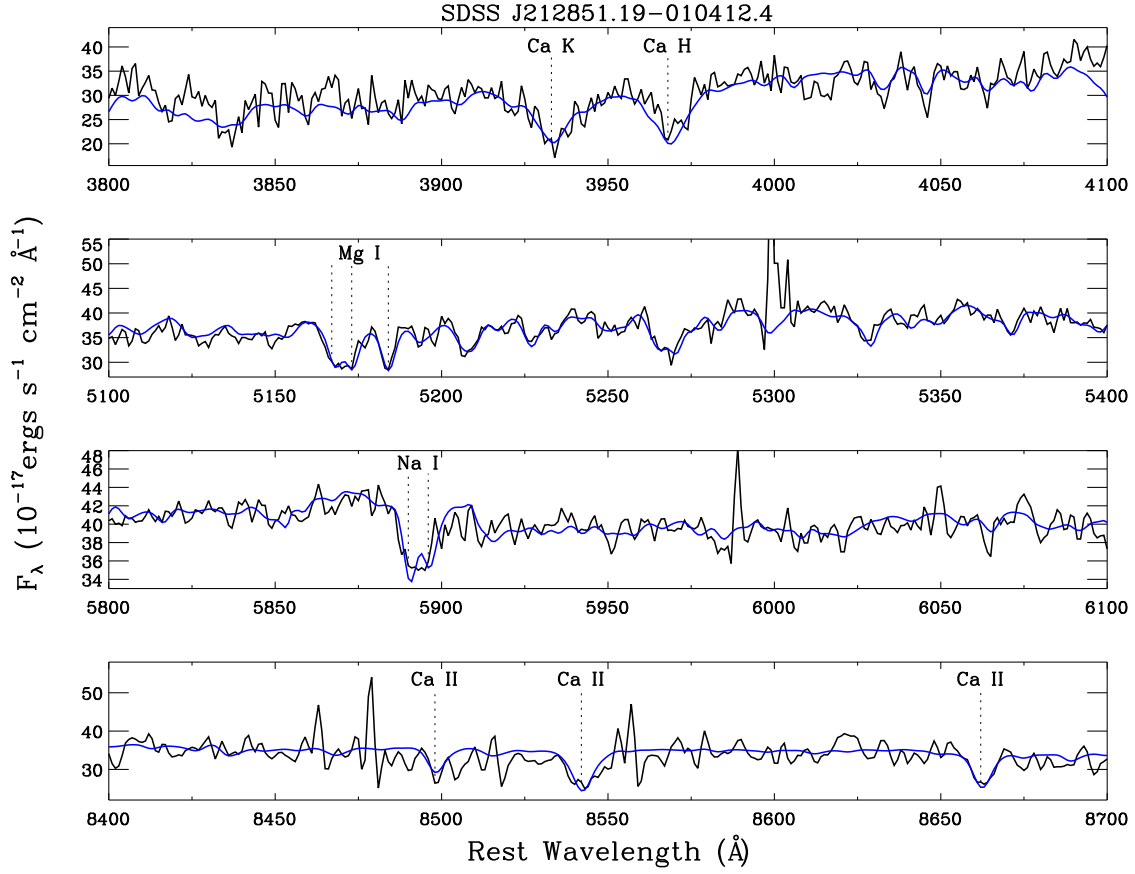


Fig. 6.— A blow-up of our best model obtained from Monte Carlo simulations for the the spectrum of J212851.19-010412.4. This fit is shown also in blue in the left panel of Fig. 5. The lines used to estimate the velocity dispersion are marked with vertical dotted lines.

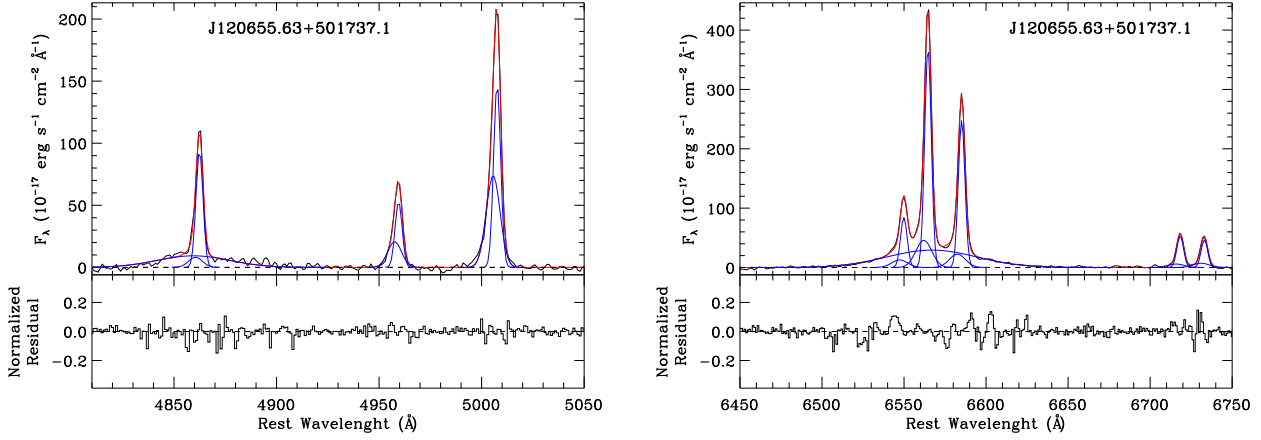


Fig. 7.— Spectral decomposition for SDSS J120655.63+501737.1. Left and right panels show our best fit obtained for the blue and red part of the spectrum, respectively. In both panels black lines correspond to the pure AGN spectrum obtained with STARLIGHT, blue lines show the Gaussian components used for the fit and red lines the best fit obtained. At the bottom of each panel the corresponding normalized residuals are shown. The $[\text{O III}]\lambda 4959, 5007$ lines and the narrow component of $\text{H}\beta$ were best fitted using 2 Gaussian components. For the broad component of $\text{H}\beta$ only one Gaussian was needed for the fit. The red part of the spectrum was modeled in a similar way, i.e., two Gaussian components for the narrow lines and one Gaussian for the broad component of $\text{H}\alpha$.

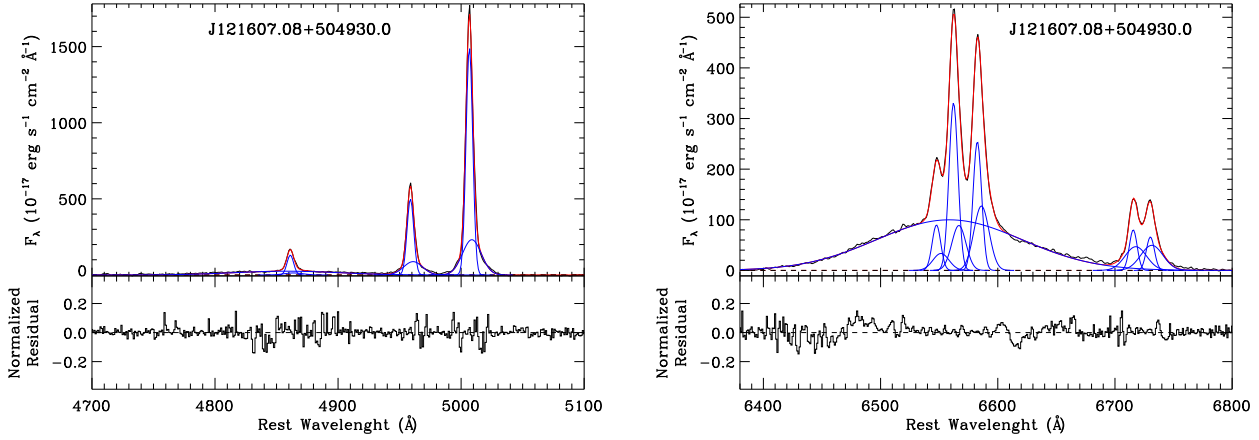


Fig. 8.— Spectral decomposition for SDSS J121607.08+504930.0. We have modeled the lines in a similar way as described in Fig. 7.

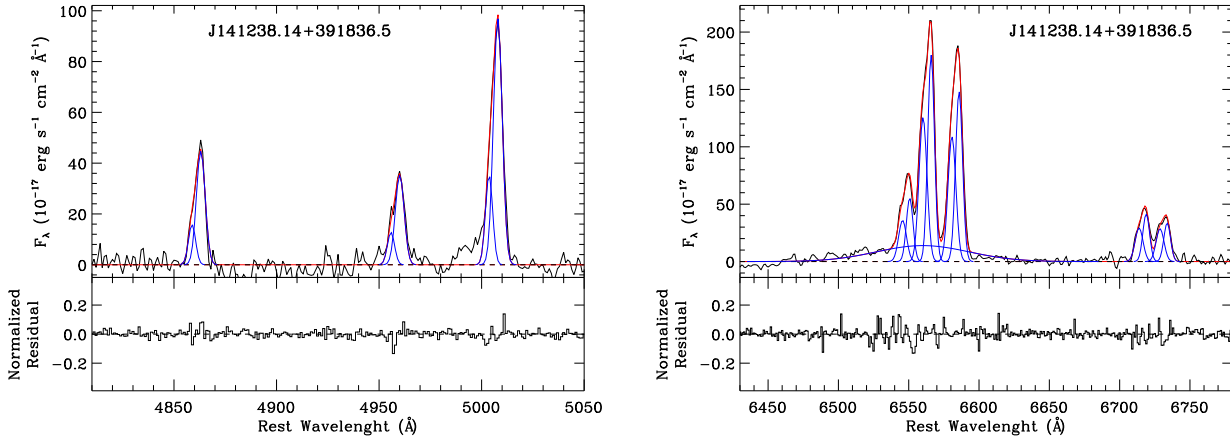


Fig. 9.— Spectral decomposition for SDSS J141238.14+391836.5. This object has also been modeled using two Gaussian components for the narrow lines. But, when fitting the broad components we found no evidence for a broad component in $H\beta$. For the red part of the spectrum a broad Gaussian component was needed for properly fitting the $H\alpha$ line, and the two Gaussian components for the narrow lines.

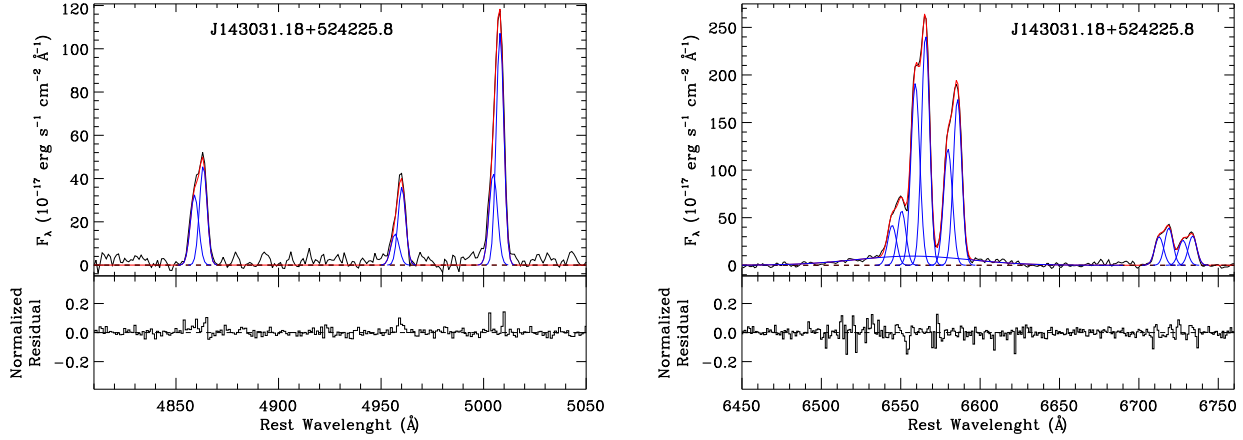


Fig. 10.— Spectral decomposition for SDSS J143031.18+524225.8. This object has been modeled similar to the one shown in Fig. 9.

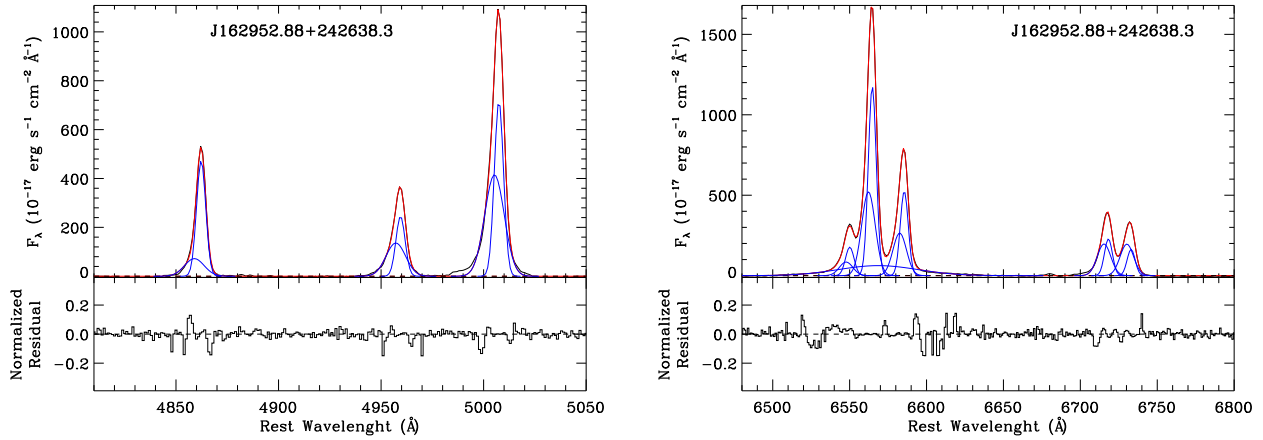


Fig. 11.— Spectral decomposition for SDSS J162952.88+242638.3. The lines were fitted using three Gaussian components for $[\text{O III}]\lambda 4959, 5007$ since it shows a wing component in addition to the two narrow components. The red part of the spectrum was fitted using two Gaussian components for the narrow lines. There is no broad component in $\text{H}\beta$, but a broad component was fitted for $\text{H}\alpha$.

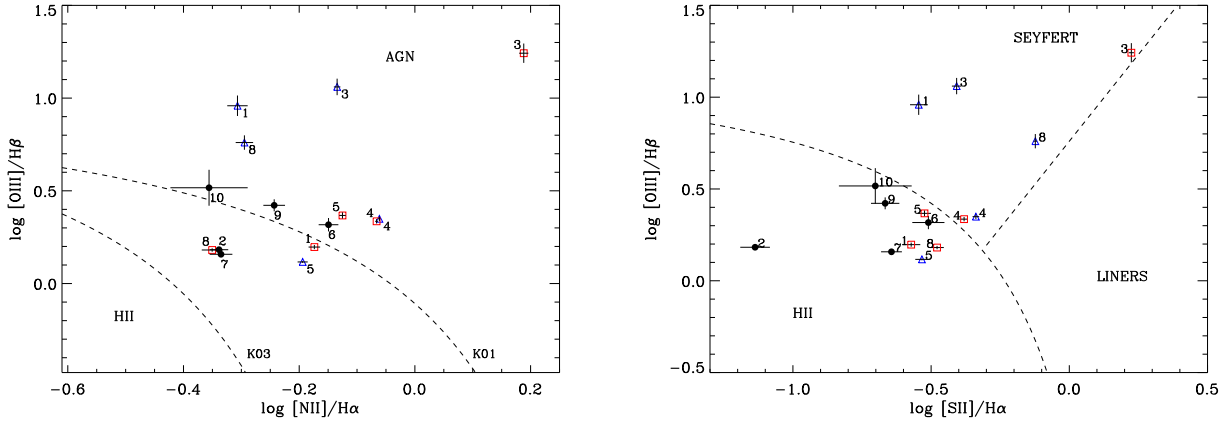


Fig. 12.— Location of the objects of the sample in two BPT diagnostic diagrams. Left side, the dotted lines come from: (Kewley et al. 2001, K01) and (Kauffmann et al. 2003, K03). Some objects are composite AGN, i.e., they lie between K01 and K03 lines, meaning that they have a Starburst galaxy (SB) plus an AGN. Filled black dots mark the locus of single-peaked objects. Objects with narrow double-peaked emission lines are shown twice since we used the ratios obtained from their red (open squares) and blue (open triangles) components. Right side, BPT diagram showing that all objects are located above the LINER region accordingly with Kewley et al. (2006). The spectral classification is presented in Table 5.

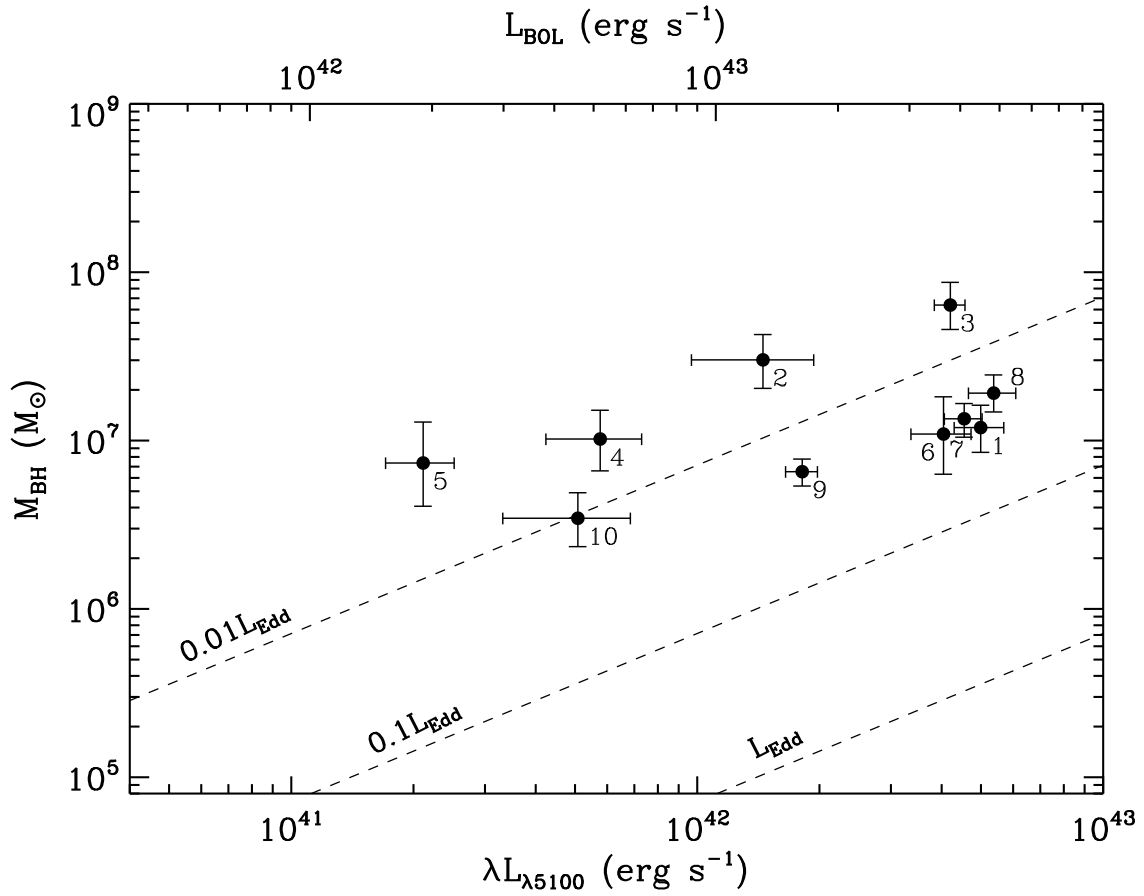


Fig. 13.— Diagram M_{BH} vs. luminosity. The upper x-axis shows the bolometric luminosity assuming $L_{bol} \sim 9\lambda L_{\lambda 5100}$.

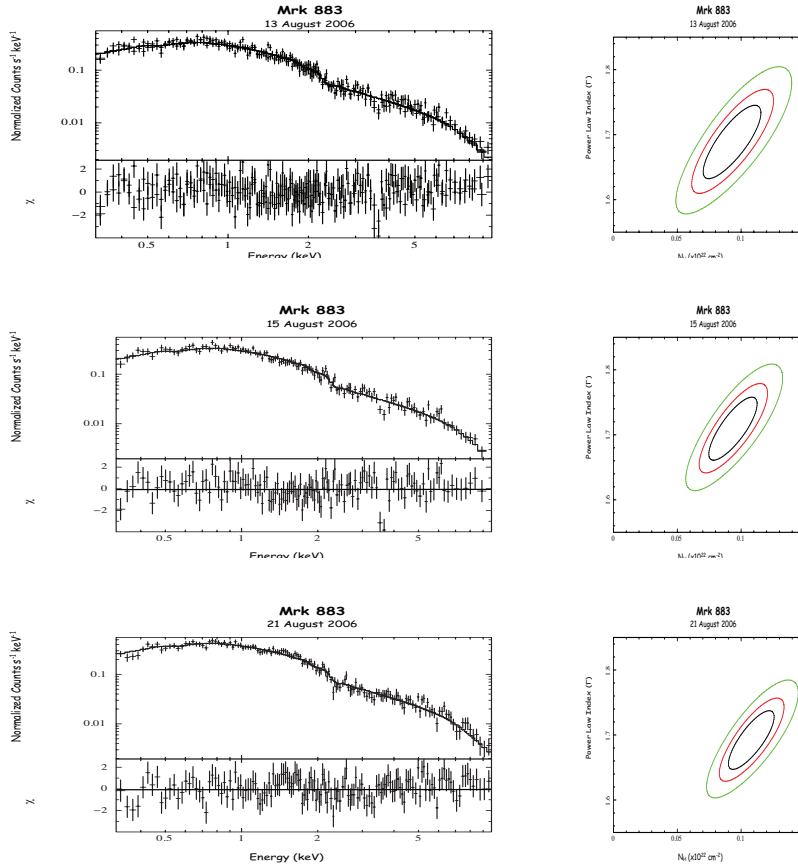


Fig. 14.— Left column: EPIC-pn observed spectra of SDSS J162952.88+242638.3 (Mrk 883) together with the best-fit model and the residuals. More details of the model can be found in Table 6. Right column: contour plots of the index of the power law and the equivalent hydrogen column density for the three XMM-Newton observations of this object. Each line corresponds to a different observation date.

Table 1. Intermediate-type AGN Sample

Galaxy #	SDSS ID	Other Name	z	D_L (Mpc)	M_g
1	J120655.63+501737.1	SBS 1204+505B	0.062	278.01	16.20
2	J121600.04+124114.3	Mrk 764	0.066	296.78	14.87
3	J121607.08+504930.0	Mrk 1469	0.031	135.92	15.27
4	J141238.14+391836.5	NGC 5515	0.026	113.58	13.78
5	J143031.18+524225.8	SBS 1428+529	0.044	194.77	15.25
6	J144049.35+505009.2	SBS 1439+510	0.117	544.65	17.28
7	J153810.05+573613.1	SBS 1537+577	0.073	329.87	15.51
8	J162952.88+242638.3	Mrk 883	0.038	167.47	15.26
9	J212851.19–010412.4	IC 1385	0.052	231.51	15.21
10	J234428.81+134946.0	...	0.068	306.21	16.32

Note. — Col. 1: galaxy identification. Col. 2: SDSS id. Col. 3: other names. Col. 4: redshift by NED. Col. 5: luminosity distance. Col. 6: Petrosiang-band magnitude given in SDSS-DR7.

Table 2. Optical Spectroscopic Parameters

Galaxy #	S/N	FWHM ($H\alpha$) (km s^{-1})	FWHM ($H\beta$) (km s^{-1})	log [O III]/ $H\beta$			log [N II]/ $H\alpha$			log [S II]/ $H\alpha$		
				blue	red	single-peak	blue	red	single-peak	blue	red	single-peak
1	13.5±0.4	2950±58	2565±284	0.96±0.06	0.20±0.01		-0.31±0.02	-0.17±0.10		-0.54±0.03	-0.57±0.03	
2	9.2±0.2	4860±158	5549±449*			0.18±0.01				-0.34±0.02		-1.14±0.05
3	8.8±0.2	6700±69	6190±739	1.06±0.04	1.24±0.05		-0.13±0.01	0.19±0.01		-0.41±0.02	0.23±0.01	
4	8.3±0.2	3551±279	4068±489*	0.35±0.01	0.34±0.01		-0.06±0.002	-0.07±0.002		-0.34±0.01	-0.38±0.01	
5	5.9±0.1	3878±341	4438±583*	0.12±0.01	0.37±0.02		-0.19±0.01	-0.13±0.01		-0.53±0.02	-0.52±0.02	
6	6.5±0.4	3194±143	2584±519			0.32±0.04				-0.15±0.02		-0.51±0.06
7	10.6±0.3	2491±38	2788±187			0.16±0.01				-0.34±0.02		-0.64±0.04
8	11.5±0.3	2776±87	3187±219*	0.76±0.04	0.18±0.01		-0.29±0.02	-0.35±0.02		-0.12±0.01	-0.48±0.02	
9	10.7±0.4	1955±25	2443±101			0.42±0.03				-0.24±0.02		-0.66±0.05
10	6.3±0.5	2094±38	2442±178			0.52±0.10				-0.36±0.07		-0.70±0.13

Note. — Col. 1: Galaxy # (cf. Table 1). Col. 2: SDSS spectra S/N obtained from STARLIGHT (Cid Fernandes et al. 2005). Col. 3: FWHM($H\alpha$) broad component. Col. 4: FWHM($H\beta$) broad component. Cols. 5-7: log [O III]/ $H\beta$ line ratios for double-peaked objects (blue and red) and for single-peaked sources. Col. 8-10: log [N III]/ $H\beta$ line ratios for double-peaked objects (blue and red) and for single-peaked sources. Col 11-13: log [S II]/ $H\alpha$ line ratios for double and single-peaked sources. Note that we mark an * in objects where the FWHM($H\beta$) was obtained using Shen et al. (2008), see text.

Table 3. Velocity differences in narrow double-peaked AGN

SDSS	J120655.63+501737.1	J121607.08+504930.0	J141238.14+391836.5	J143031.18+524225.8	J162952.88+242638.3
	(#1)	(#3)	(#4)	(#5)	(#8)
	ΔV	ΔV	ΔV	ΔV	ΔV
Line	(km s ⁻¹)	(km s ⁻¹)	(km s ⁻¹)	(km s ⁻¹)	(km s ⁻¹)
H α λ 6562.74	116 \pm 17	209 \pm 122	264 \pm 15	296 \pm 5	115 \pm 3
[N II] λ 6548	117 \pm 31	177 \pm 48	232 \pm 28	276 \pm 32	110 \pm 17
[N II] λ 6583	118 \pm 5	160 \pm 107	231 \pm 32	274 \pm 12	135 \pm 5
[S II] λ 6716	111 \pm 15	97 \pm 9	226 \pm 7	272 \pm 15	128 \pm 7
[S II] λ 6731	96 \pm 35	56 \pm 8	226 \pm 13	271 \pm 20	123 \pm 7
H β λ 4861.29	120 \pm 11	160 \pm 10	263 \pm 80	264 \pm 17	142 \pm 20
[O III] λ 4959	118 \pm 35	132 \pm 26	258 \pm 18	199 \pm 185	139 \pm 10
[O III] λ 5007	116 \pm 11	120 \pm 7	256 \pm 120	198 \pm 64	130 \pm 3
average value	114 \pm 7	139 \pm 45	245 \pm 16	256 \pm 34	128 \pm 11

Note. — Velocity differences obtained between the red and the blue Gaussian components ($\Delta V = V_{red} - V_{blue}$). Col. 1: line rest frame. Cols. 2-6: velocity differences obtained for SDSS objects J120655.63+501737.1, J121607.08+504930.0, J141238.14+391836.5, J143031.18+524225.8, and J162952.88+242638.3, respectively. Last row indicates the average ΔV value and standard deviation of each object considering all lines

Table 4. Luminosities and Eddington Rates

Galaxy #	$\lambda L_{\lambda 5100}$ (10^{41} erg s $^{-1}$)	L_{bol} (10^{42} erg s $^{-1}$)	L_{Edd} (10^{44} erg s $^{-1}$)	L_{bol}/L_{Edd} (10^{-2})
1	49.92±6.98	45±6.28	15.05±5.08	2.98±1.42
2	14.52±4.84	13.07±4.36	37.99±14.24	3.44±0.24
3	42.02±3.65	37.82±3.28	80.45±26.41	0.47±0.20
4	5.77±1.53	5.19±1.38	12.87±5.39	0.40±0.28
5	2.11±0.41	1.90±0.37	9.27±5.38	0.21±0.16
6	40.43±6.83	36.39±6.14	13.77±7.32	2.64±0.02
7	45.47±4.90	40.92±4.37	16.98±3.96	2.41±0.82
8	53.74±7.17	48.37±6.45	24.12±6.03	2.01±0.01
9	18.14±1.63	16.33±1.47	8.23±1.43	1.98±0.52
10	5.08±1.76	4.57±1.59	4.35±1.59	1.11±0.75

Note. — Col. 1: galaxy # (cf. Table 1). Col. 2: luminosity at 5100 Å measured using a continuum power-law fit. Col. 3: bolometric luminosities obtained assuming $L_{bol} = 9\lambda L_{\lambda 5100}$. Col. 4: Eddington luminosities using our estimated $M_B H$. Col. 5: Eddington ratio.

Table 5. BH Mass

Galaxy #	σ_* (km s ⁻¹)	$\log M_{BH}$ (M _⊙)	Spectral Classification	Double-peak
1	90±6	7.08± 0.14	Sy 1.8 + SB/Sy 1.5 + SB	yes
2	111±6	7.48±0.16	Sy 1.9 + SB/SB	no
3	147±7	7.81± 0.14	Sy 1.8	yes*
4	195±8	7.01± 0.18	Sy 1.9	yes*
5	165±9	6.86±0.25	Sy 1.5 + SB	yes
6	188±17	7.04±0.23	Sy 1.5 + SB	no
7	91±6	7.13±0.10	Sy 1.5 + SB	no
8	187±9	7.28±0.11	Sy 1.9 + SB	yes
9	79±6	6.82±0.08	Sy 1.5 + SB	no
10	93±11	6.54±0.16	Sy 1.8 + SB	no

Note. — Col. 1: galaxy id. (cf. Table 1). Col. 2: velocity dispersion obtained with STARLIGHT. Errors were estimated from our Monte Carlo simulation on the data, see text. Col. 3: Black hole mass estimates were obtained with the relation given by Vestergaard & Peterson (2006). Black hole mass for object #8 have to be taken with care since the host galaxy is probably a merger. Col. 4: Sy type. Col. 5: yes if it is double peak, and * shows the two dual AGN candidates found in our study.

Table 6. X-ray Spectroscopic Parameters

Obs.		Neutral Abs	Power Law	Emission Line		Goodness			Flux		Luminosity	
Day	Model	N_H	Γ	Energy	EW	χ^2_ν	d.o.f.	F-test	0.5-2 keV	2-10 keV	0.5-2 keV	2-10 keV
13	A	9±2	1.68±0.06			134.0	118		0.65 ^{+0.03} _{-0.04}	1.51 ± 0.05	2.64 ^{+0.12} _{-0.16}	4.90 ± 0.16
	B	9±2	1.69±0.06	6.4f	<170	133.9	117	35.2%				
	C	10±2	1.70±0.06	6.88 ^{+0.08} _{-0.15}	210 ⁺¹⁸⁰ ₋₁₆₀	129.0	116	87.5%				
15	A	9±2	1.71±0.05			135.0	129		0.66±0.02	1.47±0.05	2.66±0.08	4.79±0.16
	B	10±2	1.72±0.05	6.4f	210 ⁺⁹⁰ ₋₁₅₀	128.9	128	98.5%				37
	C	10±2	1.72±0.05	6.34 ^{+0.08} _{-0.10}	200 ⁺¹³⁰ ₋₁₂₀	127.3	127	97.6%				—
21	A	11±2	1.69±0.05			128.9	145		0.83±0.03	1.95±0.05	3.43±0.12	6.33±0.16
	B	11±2	1.70±0.05	6.4f	75 ⁺⁴ ₋₃	126.9	144	86.6%				
	C	11±2	1.70±0.05	6.55±0.15	150±110	123.9	143	94.1%				

Note. — Col 1: day of observations, data are from August 2006. Col 2: model A: absorbed power law; model B: absorbed power law plus a neutral iron line with the energy fixed; model C: absorbed power law plus an iron line with the energy left free to vary. Col 3: neutral absorption in units of 10^{20} cm^{-2} . Col (4): power law index. Col (5) and (6): energy in keV and equivalent width in eV, respectively. Col (7): modified reduced χ^2 . Col (8) degrees of freedom. Col (9) F-test. Col. 10 and 11: fluxes in $10^{-12} \text{ erg s}^{-1} \text{ cm}^{-2}$. Col. 12 and 13: luminosities in $10^{42} \text{ erg s}^{-1}$.